

## Article

# High pO<sub>2</sub> Flux Growth and Characterization of NdNiO<sub>3</sub> Crystals

Xiaoli Wang<sup>1</sup>, Shilei Wang<sup>1</sup>, Chao Liu<sup>1</sup>, Chuanyan Fan<sup>1</sup>, Lu Han<sup>1</sup>, Feiyu Li<sup>1</sup>, Tieyan Chang<sup>2</sup> , Yu-Sheng Chen<sup>2</sup>, Shanpeng Wang<sup>1</sup>, Xutang Tao<sup>1,\*</sup> and Junjie Zhang<sup>1,\*</sup> 

<sup>1</sup> State Key Laboratory of Crystal Materials, Shandong University, Jinan 250100, China

<sup>2</sup> NSF's ChemMatCARS, The University of Chicago, Argonne, IL 60439, USA

\* Correspondence: txt@sdu.edu.cn (X.T.); junjie@sdu.edu.cn (J.Z.)

**Abstract:** Single crystals of the perovskite nickelate NdNiO<sub>3</sub> with dimensions of up to 50 μm on edge have been successfully grown using the flux method at a temperature of 400 °C and oxygen pressure of 200 bar. The crystals were investigated by a combination of techniques, including high-resolution synchrotron X-ray single-crystal and powder diffraction and physical property measurements such as magnetic susceptibility and resistivity. Resistivity measurements revealed a metal-insulator transition (MIT) at  $T_{MIT} \sim 180$  K with apparent thermal hysteresis; however, no superlattice peaks or peak splitting below  $T_{MIT}$ , which corresponds to a structural transition from *Pbnm* to *P2<sub>1</sub>/n*, was observed. The successful growth of NdNiO<sub>3</sub> crystals at relatively low temperatures and oxygen pressure provides an alternative approach for preparing single crystals of interesting perovskites such as RNiO<sub>3</sub> (R = Sm-Lu) and parent phases of superconducting square planar nickelates.

**Keywords:** high pressure crystal growth; flux growth; perovskite; nickelate; metal-insulator transition



**Citation:** Wang, X.; Wang, S.; Liu, C.; Fan, C.; Han, L.; Li, F.; Chang, T.; Chen, Y.-S.; Wang, S.; Tao, X.; et al. High pO<sub>2</sub> Flux Growth and Characterization of NdNiO<sub>3</sub> Crystals. *Crystals* **2023**, *13*, 180. <https://doi.org/10.3390/cryst13020180>

Academic Editor: Borislav Angelov

Received: 27 December 2022

Revised: 16 January 2023

Accepted: 16 January 2023

Published: 19 January 2023



**Copyright:** © 2023 by the authors. Licensee MDPI, Basel, Switzerland. This article is an open access article distributed under the terms and conditions of the Creative Commons Attribution (CC BY) license (<https://creativecommons.org/licenses/by/4.0/>).

## 1. Introduction

The discovery of superconductivity in the thin film of Nd<sub>0.8</sub>Sr<sub>0.2</sub>NiO<sub>2</sub> by Li et al. [1] has attracted intense attention in the fields of condensed matter physics and materials science and launched the Nickel Age of Superconductivity [2–14]. Until today, superconductivity with a critical temperature ( $T_c$ ) in the range of 9–15 K has been observed in the infinite-layer R<sub>1-x</sub>M<sub>x</sub>NiO<sub>2</sub> (R = La, M = Ca, Sr; R = Pr, Nd, M = Sr) [15–19] and the quintuple-layer Nd<sub>6</sub>Ni<sub>5</sub>O<sub>12</sub> [20]. Under high static pressure,  $T_c$  has been increased to 30 K in Pr<sub>0.8</sub>Sr<sub>0.2</sub>NiO<sub>2</sub> films [21]. After 3 years of intense research, several fundamental issues still exist [2–14], including the mechanism of superconductivity, the similarity and difference between nickelate and cuprate superconductivity, whether the ground state is magnetic, and whether competing phases such as pseudogaps and strange metals exist. Single crystals are the ideal platform to solve the abovementioned open questions. However, no direct method has been found to synthesize these nickelates; instead, they were prepared by topotactical reduction through their parent compounds, i.e., Ruddlesden–Popper (RP) phases R<sub>n+1-x</sub>M<sub>x</sub>Ni<sub>n</sub>O<sub>3n+1</sub> (R = La–Nd, M = Ca, Sr,  $n = 5$ , and  $\infty$ ) [4,13].

The  $n = \infty$  RP nickelates is the well-known perovskite RNiO<sub>3</sub> (R = La–Lu, Y), which has attracted extensive attention in the past few decades in two areas: (1) as a model system for studying metal-insulator transition (MIT,  $R \neq$  La) and the lattice-charge-spin-orbital interaction [22] and (2) potential applications such as new morphological computing, bioelectronic interfaces, and electrocatalysis [23]. For RNiO<sub>3</sub> (R = Pr, Nd), antiferromagnetic ordering occurs simultaneously at  $T_{MIT}$  while for  $R^{3+} < Nd^{3+}$ ,  $T_N < T_{MIT}$ . Regarding the underlying physics behind MIT, there have been various proposals, including charge disproportionation, bipolaron condensation, and negative charge transfer, but it remains under debate [22]. In addition, type-II multiferroics have been theoretically predicted [24,25].

Single crystals of  $\text{RNiO}_3$  are in high demand in preparing infinite-layer nickelate crystals via topotactical reduction and for addressing the underlying mechanism of MIT and magnetism. Nickel ions usually exist in the divalent form, and the preparation of  $\text{RNiO}_3$  requires high oxygen pressure to stabilize the trivalent nickel ion. With the decrease of  $\text{R}^{3+}$  ions, the required oxygen pressure increases sharply.  $\text{LaNiO}_3$  and  $\text{PrNiO}_3$  single crystals have been grown using the high-pressure floating zone method under  $p\text{O}_2$  of 40 bar [26] and 290 bar [27], respectively. However, for  $\text{RNiO}_3$  whose  $\text{R}^{3+}$  is smaller than  $\text{Pr}^{3+}$ , the required oxygen pressure exceeds 300 bar, which is the highest pressure that can be achieved using a commercial floating zone furnace [28].  $\text{RNiO}_3$  crystals can also be grown using a high-pressure flux method. Among the literature [29–32], chloride or perchlorate ( $\text{NaCl}/\text{NaClO}_4/\text{KCl}/\text{KClO}_4$ ) are mostly used as the flux, and growth was conducted at a temperature of 900–1500 °C and isostatic pressure of 4–4.5 GPa. In 2021, Klein et al. [33] first successfully grew crystals of  $\text{RNiO}_3$  ( $\text{R} = \text{Nd, Sm, Gd, Dy, Y, Ho, Er, Lu}$ ) under  $p\text{O}_2 = 2000$  bar and  $T = 850$  °C using used  $\text{LiCl-KCl}$  flux. The dimensions of  $\text{NdNiO}_3$  crystals are up to 10  $\mu\text{m}$  on edge [33].

In this contribution, we report the successful growth of  $\text{NdNiO}_3$  crystals with dimensions up to 50  $\mu\text{m}$  under  $p\text{O}_2 = 200$  and  $T = 400$  °C using  $\text{NaOH-KOH}$  as flux. The crystals show a MIT as evidenced by transport measurements. High-resolution synchrotron X-ray single-crystal diffraction and high-resolution X-ray powder diffraction have been used to investigate the structural response across MIT. Our successful growth of  $\text{NdNiO}_3$  crystals using hydroxide flux at low temperature and reduced  $p\text{O}_2$  opens the door to a new opportunity for preparing single crystals of other interesting nickelates, including  $\text{RNiO}_3$  ( $\text{R} = \text{Sm-Lu}$ ), parent phases of superconducting square planar nickelates, and potential multiferroic nickelates.

## 2. Materials and Synthesis

### 2.1. High-Pressure Flux Growth of $\text{NdNiO}_3$ Crystals

$\text{NdNiO}_3$  crystals were grown using a high-pressure flux furnace designed for operation at  $T_{\text{max}} = 650$  °C and  $P_{\text{max}} = 300$  bar (Model HP45, TOP Industrie). A scheme of the reaction chamber within the furnace is shown in Figure 1.  $\text{Nd}_2\text{O}_3$  (Alfa Aesar, Haverhill, MA, USA, 99.99%) and  $\text{NiO}$  (Sigma-Aldrich, St. Louis, MO, USA, 99.99%) were used as starting materials.  $\text{Nd}_2\text{O}_3$  was baked at 900 °C for 24 h before use. A stoichiometric ratio of  $\text{Nd}_2\text{O}_3$  and  $\text{NiO}$  powder was weighted, mixed, and thoroughly ground, and then it was mixed with  $\text{NaOH/KOH}$  (molar ratio 1:1) flux in a glove box at a weight ratio of 1:10. The mixture was loaded into a Pt crucible, which was then put into the high-pressure furnace HP45. The furnace was filled with oxygen gas at room temperature so as to reach the targeted  $p\text{O}_2$  (5, 20, 40, 100, 200, or 300 bar) when the furnace was heated to 400 or 500 °C. During this process, oxygen is consumed due to the reaction of raw materials to form  $\text{NdNiO}_3$ . Therefore, when the pressure is lower than the expected value, gas was manually filled in: (1) in the range of 150–300 bar, we used a booster pump to increase the pressure (error bar 5%), and (2) below 150 bar, gas was added by opening the valve of gas cylinder. The furnace was maintained at targeted temperature and  $p\text{O}_2$  for 48 h in order to dissolve raw materials. After dwelling, the furnace was cooled down to 360 °C at the rate of 5 °C/h and then to 260 °C at 10 or 1 °C/h, followed by furnace cooling to room temperature. No gas was filled during cooling. Finally, flux was dissolved using distilled water and black polycrystals were obtained.

### 2.2. In-House X-ray Powder Diffraction (PXRD)

Bruker AXS D2 Phaser X-ray powder diffractometer was used to check phase purity. Data were collected at room temperature using  $\text{Cu-K}\alpha$  radiation ( $\lambda = 1.5418$  Å) in the  $2\theta$  range of 10–90° with a scan step of 0.02° and 0.2 s per step. Rietveld refinement was performed using TOPAS 6. Refined parameters include background (Chebychev function, 5 order), sample displacement, lattice parameters, crystallite size (L and G), strain L, and atomic positions. Thermal parameters were not refined.

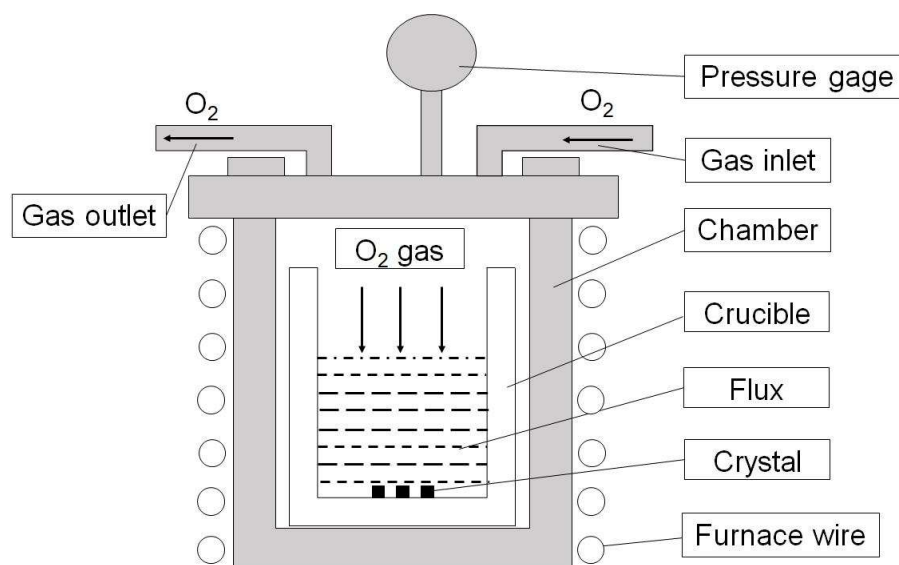


**Figure 1.** Scheme of reaction chamber within the furnace.

### 2.3. Synchrotron X-ray Single-Crystal Diffraction (SXRD)

X-ray single-crystal diffraction data were collected with a Pilatus3 X 1M (CdTe) area detector using synchrotron radiation ( $\lambda = 0.41328 \text{ \AA}$ ) at 250 K and 120 K at Beamline 15-ID-D (NSF's ChemMatCARS) at the Advanced Photon Source, Argonne National Laboratory. A piece of a single crystal with dimensions of  $0.015 \times 0.015 \times 0.015 \text{ mm}^3$  was mounted to the tip of glass fiber and measured using a Huber 3-circle diffractometer. Indexing, data reduction, and image processing were performed using Bruker APEX3 software [34].

### 2.4. High-Resolution Synchrotron X-ray Powder Diffraction (HRPXRD)

HRPXRD data were collected at Beamline 11-BM in the  $2\theta$  range of  $0.5\text{--}50^\circ$  with a step size of  $0.001^\circ$ , counting time of 0.1 s per step, and a wavelength of  $\lambda = 0.458961 \text{ \AA}$  at 295 K and  $\lambda = 0.458956 \text{ \AA}$  at 100 K. Fine-ground polycrystalline powders were loaded into a  $\phi 0.8\text{-mm}$  Kapton capillary for installation on a magnetic sample base used by the beamline sample changer. The sample was spun continuously at 5600 rpm during data collection. An Oxford Cryostream 700 Plus N<sub>2</sub> gas blower was used to control the temperature at 100 K. Rietveld refinement was performed using TOPAS 6. Refined parameters include background (Chebychev function, 5 order), zero error, lattice parameters, crystallite size (L and G), strain (L and G), atomic positions, and thermal parameters ( $B_{\text{eq}}$ ). Simple axial Model was used for axial convolutions.

### 2.5. Scanning Electron Microscopy (SEM)

SEM was used to investigate the microstructure of the crystals. SEM images were obtained with a Hitachi S-4800 microscope at 5.0 kV incident electrons.

### 2.6. Energy Dispersive Spectrometer (EDS)

The X-ray spectrometer EDAX GENESIS XM2 SYSTEM 60x on S-4800 was used for qualitative and quantitative analysis of the as-grown crystals. The experiment was carried out on a  $0.040 \times 0.030 \times 0.030 \text{ mm}^3$  crystal.

### 2.7. Electrical Transport

Resistivity was measured using the standard four-probe method. The single crystals were too small to make four contacts, so instead, crystals were ground into powders, pressed into thin pellets, and then annealed under different conditions. The pellets were cut into thin bars for making four contacts with silver paint. The temperature was controlled

using the Quantum Design Physical Properties Measurement System (Dynacool-9) in the range of 2–300 K.

### 2.8. Magnetic Susceptibility

The DC magnetization of the samples was measured using a PPMS Dynacool-9. The polycrystalline sample was packed in a clear plastic capsule. The sample was cooled in zero fields to 2 K, and DC magnetization data were recorded on warming (3 K/min). We also measured the magnetization of the empty capsule under the same conditions, which was negligible compared with the sample.

## 3. Results and Discussion

### 3.1. High $pO_2$ Single Crystal Growth

The flux method was used to grow NdNiO<sub>3</sub> crystals. We first consider the LiCl-KCl flux system, as Klein et al. [33] grew NdNiO<sub>3</sub> crystals of 10 μm under 2000 bar at 850 °C, and Prakash et al. [35] successfully synthesized polycrystalline powders of EuNiO<sub>3</sub> and GdNiO<sub>3</sub> at 180 bar O<sub>2</sub>. Higher  $pO_2$  is needed for RNiO<sub>3</sub> with smaller R ions [26,27], thus we expect to grow NdNiO<sub>3</sub> crystals below  $pO_2 = 180$  bar. Unfortunately, we failed to grow crystals but found erosion in our furnace due to the reaction between LiCl-KCl and the chamber (Ni-superalloy).

We noticed that the mixture of NaOH/KOH (molar ratio 1:1) has a low melting point of ~170 °C, which could possibly lower the growth temperature of NdNiO<sub>3</sub> significantly and reduce defects in the as-grown crystals. In addition, we found that single crystals of YBa<sub>2</sub>Cu<sub>4</sub>O<sub>8</sub> and NaNiO<sub>2</sub> were successfully grown by Song et al. [36] and Brion et al. [37], respectively, using such a hydroxide flux system. Initially, we attempted to grow NdNiO<sub>3</sub> at  $pO_2 = 20$  bar at 400 °C. Black powders with tiny shiny crystals of ~10 μm were obtained. Figure 2 shows the Rietveld refinement of in-house powder X-ray diffraction data with  $R_{wp} = 6.52\%$  (see Table S1 for Rietveld details). All peaks can be indexed in the space group *Pbnm* with lattice parameters  $a = 5.4019(3)$  Å,  $b = 5.3697(3)$  Å,  $c = 7.6009(5)$  Å, which are comparable to the results reported by Wang et al. [38]. Therefore, we obtained the same size of NdNiO<sub>3</sub> crystals at less than a half in temperature and two orders lower in oxygen pressure of Klein et al [33].

We then optimized the growth conditions of NdNiO<sub>3</sub>, including  $pO_2$ , dwelling time, dwelling temperature, and cooling rate (see Table 1) in order to improve the dimensions and quality of crystals. We first optimized the dwelling time under  $pO_2 = 20$  bar, and the content of the NiO impurity phase in the product decreased significantly after the dwelling time was extended from 24 to 48 h; there was no obvious improvement after 48 h. Therefore, the dwelling time was selected as 48 h in the subsequent experiments. We then turned to optimizing  $pO_2$ . Unexpectedly, the pure phase of NdNiO<sub>3</sub> could be obtained at the lowest oxygen pressure of 5 bar, but the overall particles were small and no crystals could be observed under the microscope using 185 times magnification (Figure 3a). When the oxygen pressure was increased to 100 bar, prismatic crystals appeared (see Figure 3b). With the increase of  $pO_2$  to 200 bar, the crystal size and morphology are remarkably improved (Figure 3c). Further increasing the  $pO_2$  to 300 bar, the crystal size increased to a small extent (not shown). Figure 3d presents the crystal size as a function of  $pO_2$  under the same conditions: NdNiO<sub>3</sub>/flux = 1:10 (weight), dwelling time 48 h at 400 °C, and cooling rate 10 °C/h. As can be seen, the size of crystals increases significantly as  $pO_2$  increases and improves limitedly beyond 200 bar. For dwelling temperature, we went to 500 °C under  $pO_2$  of 300 bar, and the dimensions of the obtained NdNiO<sub>3</sub> were the same level as 400 °C, while the corrosion of the flux to crucible was much worse. Furthermore, NaOH in the flux reacted with NiO to form Na<sub>0.6</sub>Ni<sub>3</sub>O<sub>5.4</sub> impurities. Thus, we determined 200 bar as the optimized  $pO_2$ . We further slowed down the cooling rate to 1 °C/h, and finally obtained shiny NdNiO<sub>3</sub> crystals with a maximum size of about 50 μm (Figure 3e). SEM showed that the crystal had a regular appearance without obvious defects (Figure 3f). The composition of the crystals was estimated using EDS Figure S1 (See Supplementary Materials). The EDS

data showed that the crystals contained Nd, Ni, and O elements, and the molar ratio of Nd: Ni is close to 1.

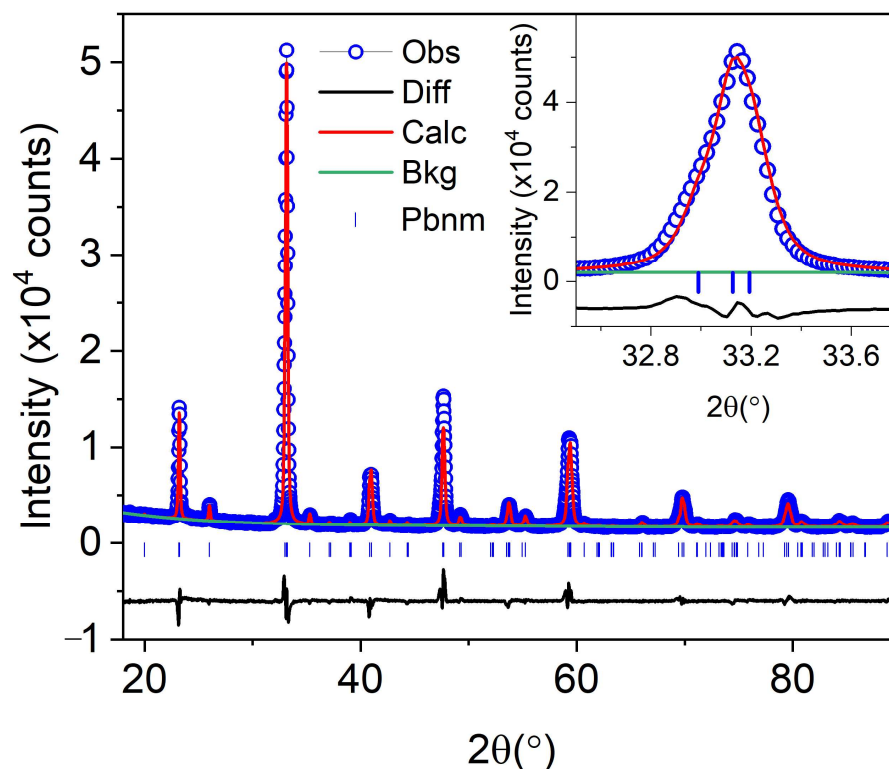


**Figure 2.** Rietveld refinement of in-house PXRD ( $\lambda = 1.5418 \text{ \AA}$ ) of pulverized as-grown crystals of  $\text{NdNiO}_3$ . Obs: observed intensity; Diff: difference; Calc: calculated intensity; Bkg: background.

**Table 1.** Growth conditions of  $\text{NdNiO}_3$  crystals.

T (°C)	pO <sub>2</sub> (Bar)	Dwelling Time (h)	Cooling Rate (°C/h)	Phase (s)	Crystal Size (μm)
400	5	24	10	$\text{NdNiO}_3 + \text{NiO}$ (trace)	<5
400	20	24	10	$\text{NdNiO}_3 + \text{NiO}$ (trace)	<5
400	20	48	10	$\text{NdNiO}_3$	<5
400	100	48	10	$\text{NdNiO}_3$	5–15
400	200	48	10	$\text{NdNiO}_3$	15–25
400	300	48	10	$\text{NdNiO}_3$	15–28
500	300	48	10	$\text{NdNiO}_3 + \text{Na}_{0.6}\text{Ni}_3\text{O}_{5.4}$	15–28
400	200	48	1	$\text{NdNiO}_3$	20–50

### 3.2. Physical Properties

**Resistivity.** To check if our crystals show metal-insulator transition, we performed resistivity measurements. As the crystals are not large enough, we measured resistivity on polycrystalline thin bars using the four-probe method. Figure 4 shows the resistivity of  $\text{NdNiO}_3$  as a function of temperature on heating and cooling from three samples: (a) annealed at 650 °C for 48 h under pO<sub>2</sub> = 280 bar, (b) annealed at 800 °C for 12 h under pO<sub>2</sub> = 1 bar (see Figure S2 for PXRD), and (c) initially annealed at 800 °C for 12 h under pO<sub>2</sub> = 1 bar and then at 650 °C for 12 h under pO<sub>2</sub> = 280 bar. All three samples exhibit metal-insulator transition, although the transition temperature is a bit lower compared with 196 K reported in Ref. [33]. This  $T_{\text{MIT}}$ -reduced behavior is consistent with previously reported polycrystalline samples that contain oxygen vacancies [39]. Sample (a) shows a large hysteresis and re-enters a metallic state at a lower temperature. This re-entry behavior has also been observed in  $\text{PrNiO}_3$  single crystals, which was attributed to the presence of

oxygen vacancies [27]. The existence of oxygen deficiency in our samples is not unexpected as this is a common phenomenon in perovskite oxides and the  $pO_2$  we used for crystal growth is one order smaller than Klein et al. [33]. The above three samples are expected to have different oxygen contents, and the oxygen content of as-grown crystals should fall into their range; thus, one expects to see metal-insulator transition in the as-grown crystals. To achieve stoichiometric oxygen contents, annealing at high  $pO_2$  and longer time are needed.

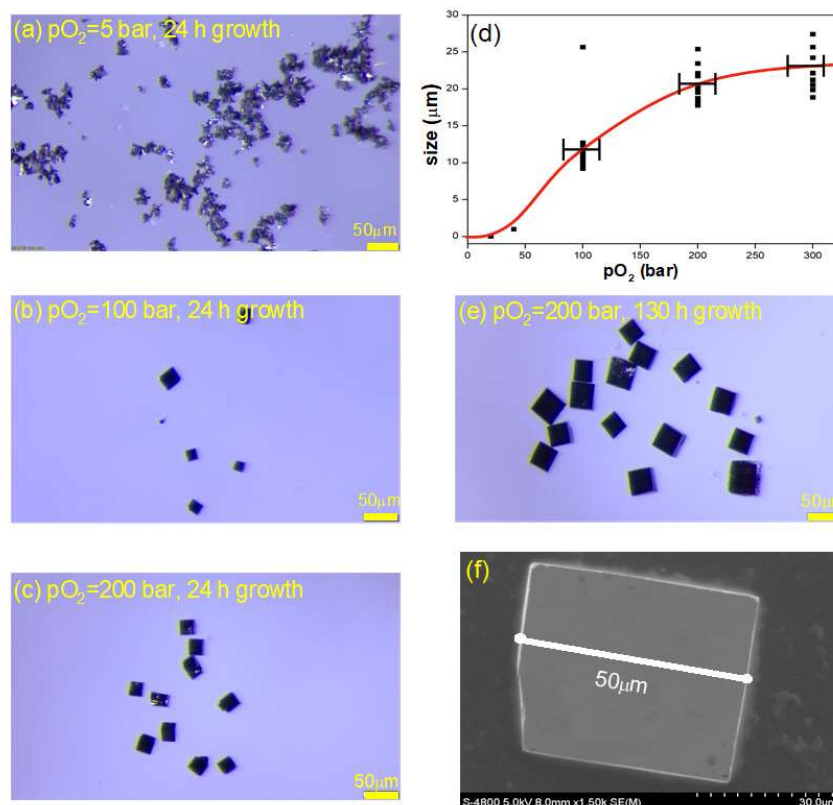


**Figure 3.** NdNiO<sub>3</sub> crystals grown under different  $pO_2$ . (a)  $pO_2 = 5$  bar, growth time 24 h; (b)  $pO_2 = 100$  bar, growth time 24 h; (c)  $pO_2 = 200$  bar, growth time 24 h. (d) The relationship between grain size and  $pO_2$  under the same growth conditions (Error bars represent the oxygen pressure deviation, and the red curve is only a guide for the eye); (e)  $pO_2 = 200$  bar, growth time 130 h; (f) SEM image of NdNiO<sub>3</sub>.

**Magnetic susceptibility.** Complementary to transport properties, magnetic measurements offer an additional way to assess the properties of our sample. It was reported that antiferromagnetic order occurs concomitantly with MIT for NdNiO<sub>3</sub> [22]. The temperature dependent DC magnetic susceptibility ( $\chi$ ) and the inverse magnetic susceptibility ( $1/\chi$ ) of as-grown NdNiO<sub>3</sub> and annealed at 650 °C for 48 h under  $pO_2 = 280$  bar are shown in Figure 5. No anomaly, discontinuity, or change in slope, which would mark the onset of magnetic ordering, was observed down to 2 K. This is likely because the magnetic susceptibility is dominated by the paramagnetic contribution of Nd<sup>3+</sup>, which mask the weak signal of the Ni sublattice. A Curie–Weiss fit to the as-grown data in the range of 200–300 K,  $\chi = C/(T-\theta)$ , where  $C$  and  $\theta$  are the Curie and Weiss constants, respectively, yields  $C = 2.127$  emu K mol<sup>-1</sup> and  $\theta = -69.6$  K. The resulting effective moment is  $\mu_{\text{eff}} = 3.74$   $\mu_B$ /f.u., which is close to the expected value of 3.89  $\mu_B$ /f.u. of the free ion Nd<sup>3+</sup>. The large negative value of the Weiss constant indicates strong antiferromagnetic interactions.

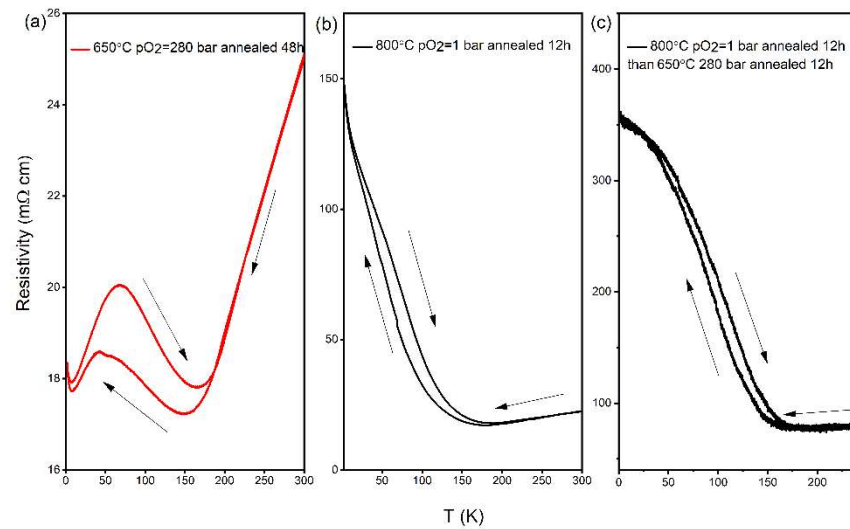


**Figure 4.** The resistivity of NdNiO<sub>3</sub> from three samples: (a) annealed at 650 °C for 48 h under pO<sub>2</sub> = 280 bar, (b) annealed at 800 °C for 12 h under pO<sub>2</sub> = 1 bar, and (c) initially annealed at 800 °C for 12 h under pO<sub>2</sub> = 1 bar and then at 650 °C for 12 h under pO<sub>2</sub> = 280 bar. Arrow indicates heating/cooling process.

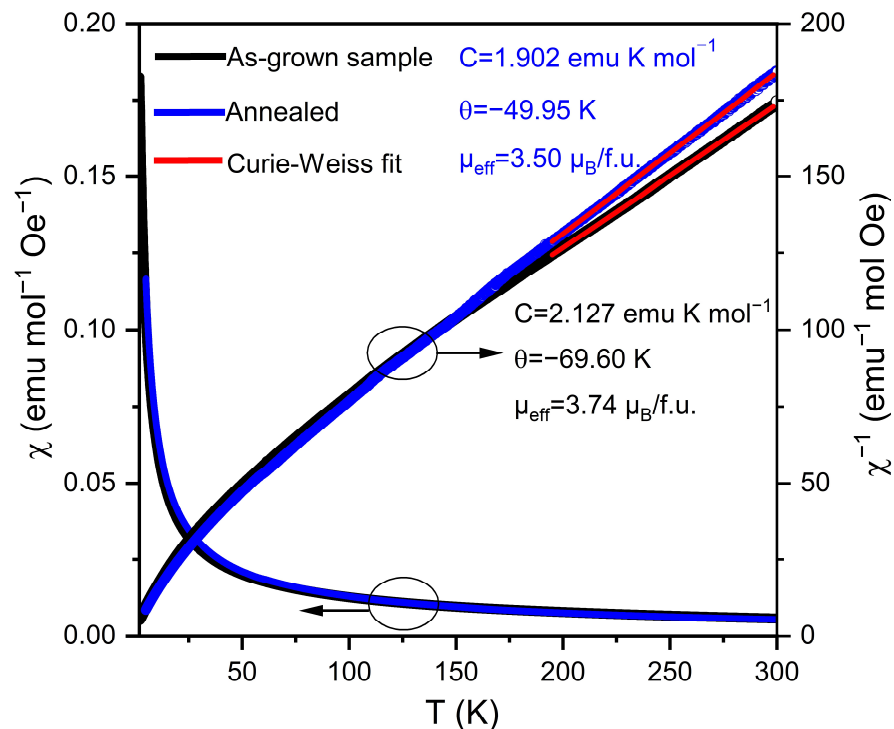


**Figure 5.** DC susceptibility  $\chi$  (left) and inverse magnetic susceptibility  $1/\chi$  (right) for as-grown NdNiO<sub>3</sub>, and NdNiO<sub>3</sub> annealed at 650 °C for 48 h under pO<sub>2</sub> = 280 bar. The symbols are the experimental data and the red lines are the Curie–Weiss fit.

### 3.3. Structural Study at Various Temperatures

Perovskite nickelates (R = Pr–Lu) exhibit an MIT from a high-temperature metallic state to a low-temperature antiferromagnetic insulator. It has been reported that NdNiO<sub>3</sub> has subtle  $Pbnm \rightarrow P2_1/n$  symmetry breaking and associated Ni site splitting below  $T_{MIT}$  [22]. To check the monoclinic distortion and possible orbital ordering [40], we have performed high-resolution X-ray single-crystal and powder diffraction using synchrotron radiation.

We found our NdNiO<sub>3</sub> single crystals are twinned even at room temperature, resulting in a pseudocubic lattice with an average lattice parameter of  $a \sim 7.6$  Å in our synchrotron X-ray single-crystal diffraction at 15-ID-D. This is understandable because, in the two translation symmetry reductions going from the SrTiO<sub>3</sub> structure, space group  $Pm\bar{3}m$ , to the orthorhombically distorted GdFeO<sub>3</sub> type, space group  $Pbnm$ , twinning is highly probable, according to the Bärnighausen tree for the various perovskite superstructures. Figure 6 shows the pseudocubic ( $hk0$ ), ( $hk1$ ), and ( $hk2$ ) planes measured by single-crystal X-ray diffraction at 120 and 250 K. There are no superlattice peaks below MIT, consistent with the lack of orbital ordering reported in Ref. [41].

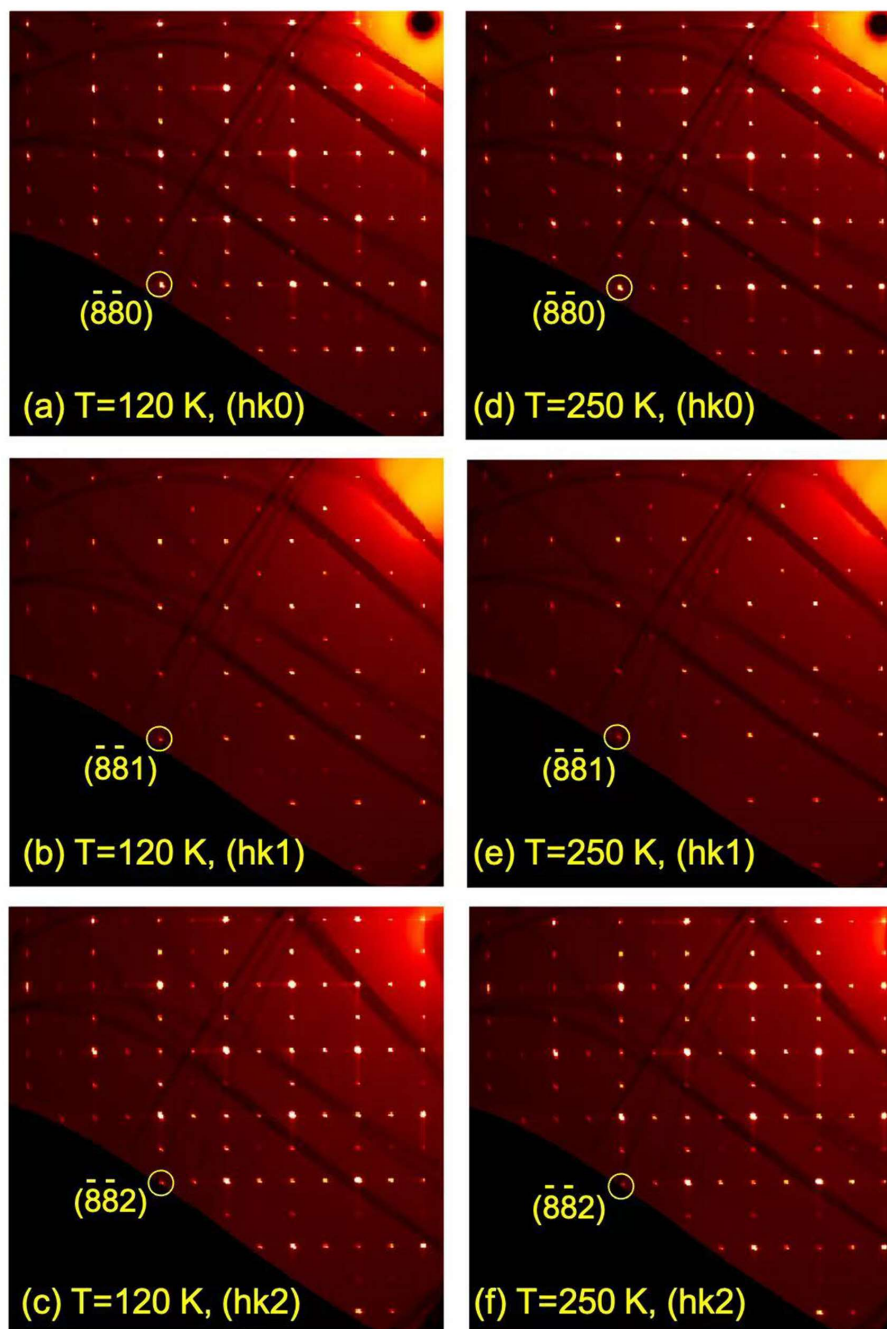


**Figure 6.** (a) Pseudocubic ( $hk0$ ) planes ( $a \sim 7.6$  Å) of as-grown NdNiO<sub>3</sub> measured by single-crystal X-ray diffraction at 120 K; (b) Pseudocubic ( $hk1$ ) planes at 120 K; (c) Pseudocubic ( $hk2$ ) planes at 120 K; (d) Pseudocubic ( $hk0$ ) planes at 250 K; (e) Pseudocubic ( $hk1$ ) planes at 250 K; (f) Pseudocubic ( $hk2$ ) planes at 250 K.

Due to twinning and possible subtle structural change across MIT, we turn to synchrotron X-ray high-resolution powder diffraction to check if any peak splitting. Synchrotron diffraction data were collected at 295 and 100 K at 11-BM at the Advanced Photon Source, Argonne National Laboratory. Tables S2–S4 list details of Rietveld refinements and obtained crystallographic data such as unit cell parameters and atomic positions. At 295 K, the diffraction pattern is in good agreement with  $Pbnm$ , and Rietveld refinement converged to  $R_{wp} = 14.88\%$  and  $GOF = 2.34$ . Our refinement shows that there are 3.99 (4)%wt NiO impurities in the sample (Figure S3a). For the diffraction data of 100 K, we fitted the data using both the orthorhombic  $Pbnm$  model and the monoclinic  $P2_1/n$  model, and slight improvement was obtained using the latter model (Figure S3b–c). Compared with the 50 K diffraction data in the literature [42], we did not observe a clear splitting of the  $(40\bar{4})/(404)$  reflections that signals the lowering symmetry to  $P2_1/n$  (Figure 7). This may be because the structural phase transition is too subtle to be detected at 100 K, and a lower temperature may be needed.

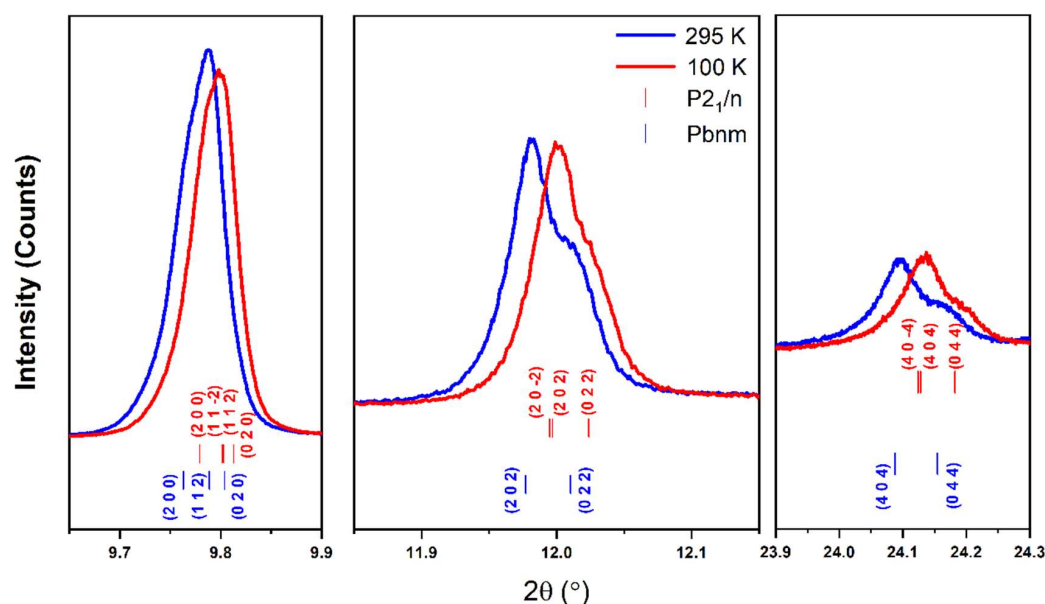


**Figure 7.** High-resolution synchrotron X-ray powder diffraction intensities of as-grown  $\text{NdNiO}_3$  in the  $2\theta$  range of  $9.65\text{--}9.9^\circ$ ,  $11.85\text{--}12.15^\circ$ , and  $23.9\text{--}24.3^\circ$  measured at 100 K ( $\lambda = 0.458956 \text{ \AA}$ ) and 295 K ( $\lambda = 0.458961 \text{ \AA}$ ). Blue (bottom) and red (top) bars correspond to  $Pbnm$  and  $P2_1/n$ , respectively.

#### 4. Conclusions

We have successfully grown  $\text{NdNiO}_3$  single crystals with dimensions of up to  $50 \mu\text{m}$  on edge at  $400^\circ\text{C}$  and 200 bar oxygen pressure using the KOH-NaOH flux system. The grown crystals have well-defined faces and regular, slightly truncated prismatic habits. Compared with previous flux systems, the hydroxide flux system significantly reduces the growth temperature and oxygen pressure while obtaining larger  $\text{NdNiO}_3$  single crystals. A clear metal-insulator transition was observed in resistivity. In contrast, no superlattice peaks were observed in synchrotron X-ray single-crystal diffraction at 120 K, nor was peak splitting found in high-resolution synchrotron X-ray powder diffraction at 100 K. The absence of the  $(40\bar{4})/(404)$  peak splitting may be due to too subtle structural change across MIT and measurements at liquid helium temperature may be needed. Finally, the high  $\text{pO}_2$  flux growth method described here provides an alternative approach for preparing single crystals of interesting perovskites, including parent phases of superconducting infinite nickelates and potential multiferroic nickelates, at a relatively low temperature and oxygen pressure [24,25].

**Supplementary Materials:** The following supporting information can be downloaded at: <https://www.mdpi.com/article/10.3390/cryst13020180/s1>, Figure S1. Elemental analysis for NdNiO<sub>3</sub> crystals; Figure S2. In-house X-ray powder diffraction for annealed NdNiO<sub>3</sub> sample; Figure S3. (a) Synchrotron X-ray high-resolution powder diffraction pattern for NdNiO<sub>3</sub> at 295 K with Rietveld refinement using the orthorhombic *Pbnm* symmetry (the purple vertical bar corresponds to the NiO impurity). (b) Synchrotron X-ray high-resolution powder diffraction pattern for NdNiO<sub>3</sub> at 100 K with Rietveld refinement using the monoclinic *P2<sub>1</sub>/n* symmetry. (c) Synchrotron X-ray high-resolution powder diffraction pattern for NdNiO<sub>3</sub> at 100 K with Rietveld refinement using the orthorhombic *Pbnm* symmetry (the inset is observed and calculated powder diffraction intensities around the orthorhombic (044) / (404) pair of reflections); Tables S1–S4. Unit cell parameters and atomic coordinates for NdNiO<sub>3</sub> as obtained from Rietveld refinements to in-house and synchrotron X-ray powder diffraction patterns. The xy data of Figure 7 and Figure S3 are uploaded as Supplementary Materials (in Excel format).

**Author Contributions:** Conceptualization, X.T. and J.Z.; Formal analysis, X.W. and J.Z.; Funding acquisition, X.T. and J.Z.; Investigation, X.W., S.W. (Shilei Wang), C.L., C.F., L.H., F.L., T.C., Y.-S.C., and S.W. (Shanpeng Wang); Methodology, J.Z.; Resources, Y.-S.C., S.W. (Shanpeng Wang) and J.Z.; Supervision, J.Z.; Validation, J.Z., X.W., C.L., C.F., L.H., and F.L.; Writing—original draft, X.W.; Writing—review & editing, J.Z.. All authors have read and agreed to the published version of the manuscript.

**Funding:** Work at Shandong University was supported by the National Natural Science Foundation of China (12074219, 51932004, 61975098), the National Key Research and Development Program of China (2016YFB1102201, 2018YFB0406502), the Natural Science Foundation of Shandong (ZR202105230005), the 111 Project 2.0 (BP2018013), the QiLu Young Scholars Program of Shandong University, the TaiShan Scholars Program of Shandong Province (tsqn201909031), the Crystal Materials and Industrialization Joint Innovation Laboratory of Shandong University and Shandong Institutes of Industrial Technology (Z1250020003), and the Project for Scientific Research Innovation Team of Young Scholars in Colleges and Universities of Shandong Province (2021KJ093). NSF's ChemMatCARS, Sector 15 at the Advanced Photon Source (APS), Argonne National Laboratory (ANL) is supported by the Divisions of Chemistry (CHE) and Materials Research (DMR), National Science Foundation, under grant number NSF/CHE- 1834750. Use of APS, an Office of Science User Facility operated for the U.S. Department of Energy (DOE) Office of Science by ANL, was supported by the U.S. DOE under Contract No. DE-AC02-06CH11357.

**Data Availability Statement:** The data that support the plots within this paper and other findings of this study are available from the corresponding author on reasonable request.

**Acknowledgments:** J.Z. and X.W. thank Saul H. Lapidus for his help with the high-resolution powder diffraction experiment at 11-BM, APS.

**Conflicts of Interest:** The authors declare no conflict of interest.

## References

1. Li, D.; Lee, K.; Wang, B.Y.; Osada, M.; Crossley, S.; Lee, H.R.; Cui, Y.; Hikita, Y.; Hwang, H.Y. Superconductivity in an infinite-layer nickelate. *Nature* **2019**, *572*, 624–627. [[CrossRef](#)]
2. Chow, L.E.; Ariando, A. Infinite-Layer Nickelate Superconductors: A Current Experimental Perspective of the Crystal and Electronic Structures. *Front. Phys.* **2022**, *10*, 834658. [[CrossRef](#)]
3. Mitchell, J.F. A Nickelate Renaissance. *Front. Phys.* **2021**, *9*, 813483. [[CrossRef](#)]
4. Bernardini, F.; Iglesias, L.; Bibes, M.; Cano, A. Thin-Film Aspects of Superconducting Nickelates. *Front. Phys.* **2022**, *10*, 828007. [[CrossRef](#)]
5. Botana, A.S.; Bernardini, F.; Cano, A. Nickelate superconductors: An ongoing dialog between theory and experiments. *J. Exp. Theor. Phys.* **2021**, *132*, 618–627. [[CrossRef](#)]
6. Botana, A.S.; Lee, K.-W.; Norman, M.R.; Pardo, V.; Pickett, W.E. Low Valence Nickelates: Launching the Nickel Age of Superconductivity. *Front. Phys.* **2022**, *9*, 813532. [[CrossRef](#)]
7. Gu, Q.; Wen, H.-H. Superconductivity in nickel-based 112 systems. *Innovation* **2022**, *3*, 100202. [[CrossRef](#)] [[PubMed](#)]
8. Hepting, M.; Dean, M.P.M.; Lee, W.-S. Soft X-ray Spectroscopy of Low-Valence Nickelates. *Front. Phys.* **2021**, *9*, 808683. [[CrossRef](#)]
9. Ji, Y.; Liu, J.; Li, L.; Liao, Z. Superconductivity in infinite layer nickelates. *J. Appl. Phys.* **2021**, *130*, 060901. [[CrossRef](#)]
10. Jiang, M. Relevance of 3D multiplet structure in nickelate and cuprate superconductors. *Chin. Phys. B* **2021**, *30*, 107103. [[CrossRef](#)]

11. Li, D. The discovery and research progress of the nickelate superconductors. *Sci. Sin. Phys. Mech. Astron.* **2021**, *51*, 047405. [[CrossRef](#)]
12. Nomura, Y.; Arita, R. Superconductivity in infinite-layer nickelates. *Rep. Prog. Phys.* **2022**, *85*, 052501. [[CrossRef](#)] [[PubMed](#)]
13. Zhang, J.; Tao, X. Review on quasi-2D square planar nickelates. *CrystEngComm* **2021**, *23*, 3249–3264. [[CrossRef](#)]
14. Zhou, X.; Qin, P.; Feng, Z.; Yan, H.; Wang, X.; Chen, H.; Meng, Z.; Liu, Z. Experimental progress on the emergent infinite-layer Ni-based superconductors. *Mater. Today* **2022**, *55*, 170–185. [[CrossRef](#)]
15. Li, D.; Wang, B.Y.; Lee, K.; Harvey, S.P.; Osada, M.; Goodge, B.H.; Kourkoutis, L.F.; Hwang, H.Y. Superconducting Dome in Nd<sub>1-x</sub>Sr<sub>x</sub>NiO<sub>2</sub> Infinite Layer Films. *Phys. Rev. Lett.* **2020**, *125*, 027001. [[CrossRef](#)] [[PubMed](#)]
16. Zeng, S.; Li, C.; Chow, L.E.; Cao, Y.; Zhang, Z.; Tang, C.S.; Yin, X.; Lim, Z.S.; Hu, J.; Yang, P.; et al. Superconductivity in infinite-layer nickelate La<sub>1-x</sub>Ca<sub>x</sub>NiO<sub>2</sub> thin films. *Sci. Adv.* **2022**, *8*, eabl9927. [[CrossRef](#)] [[PubMed](#)]
17. Zeng, S.; Tang, C.S.; Yin, X.; Li, C.; Li, M.; Huang, Z.; Hu, J.; Liu, W.; Omar, G.J.; Jani, H.; et al. Phase Diagram and Superconducting Dome of Infinite-Layer Nd<sub>1-x</sub>Sr<sub>x</sub>NiO<sub>2</sub> Thin Films. *Phys. Rev. Lett.* **2020**, *125*, 147003. [[CrossRef](#)] [[PubMed](#)]
18. Osada, M.; Wang, B.Y.; Goodge, B.H.; Lee, K.; Yoon, H.; Sakuma, K.; Li, D.; Miura, M.; Kourkoutis, L.F.; Hwang, H.Y. A superconducting praseodymium nickelate with infinite layer structure. *Nano Lett.* **2020**, *20*, 5735–5740. [[CrossRef](#)]
19. Osada, M.; Wang, B.Y.; Goodge, B.H.; Harvey, S.P.; Lee, K.; Li, D.; Kourkoutis, L.F.; Hwang, H.Y. Nickelate Superconductivity without Rare-Earth Magnetism: (La,Sr)NiO<sub>2</sub>. *Adv. Mater.* **2021**, *33*, e2104083. [[CrossRef](#)]
20. Pan, G.A.; Ferenc Segedin, D.; LaBollita, H.; Song, Q.; Nica, E.M.; Goodge, B.H.; Pierce, A.T.; Doyle, S.; Novakov, S.; Cordova Carrizales, D.; et al. Superconductivity in a quintuple-layer square-planar nickelate. *Nat. Mater.* **2022**, *21*, 160–164. [[CrossRef](#)]
21. Wang, N.N.; Yang, M.W.; Yang, Z.; Chen, K.Y.; Zhang, H.; Zhang, Q.H.; Zhu, Z.H.; Uwatoko, Y.; Gu, L.; Dong, X.L.; et al. Pressure-induced monotonic enhancement of T<sub>c</sub> to over 30 K in superconducting Pr<sub>0.82</sub>Sr<sub>0.18</sub>NiO<sub>2</sub> thin films. *Nat. Commun.* **2022**, *13*, 4367. [[CrossRef](#)]
22. Catalano, S.; Gibert, M.; Fowlie, J.; Íñiguez, J.; Triscone, J.M.; Kreisel, J. Rare-earth nickelates RNiO<sub>3</sub>: Thin films and heterostructures. *Rep. Prog. Phys.* **2018**, *81*, 046501. [[CrossRef](#)]
23. Zhang, Z.; Sun, Y.; Zhang, H.-T. Quantum nickelate platform for future multidisciplinary research. *J. Appl. Phys.* **2022**, *131*, 120901. [[CrossRef](#)]
24. Ardizzone, I.; Teyssier, J.; Crassee, I.; Kuzmenko, A.B.; Mazzone, D.G.; Gawryluk, D.J.; Medarde, M.; van der Marel, D. Raman spectroscopic evidence for multiferroicity in rare earth nickelate single crystals. *Phys. Rev. Res.* **2021**, *3*, 033007. [[CrossRef](#)]
25. Giovannetti, G.; Kumar, S.; Khomskii, D.; Picozzi, S.; van den Brink, J. Multiferroicity in rare-earth nickelates RNiO<sub>3</sub>. *Phys. Rev. Lett.* **2009**, *103*, 156401. [[CrossRef](#)]
26. Zhang, J.; Zheng, H.; Ren, Y.; Mitchell, J.F. High-pressure floating-zone growth of perovskite nickelate LaNiO<sub>3</sub> single crystals. *Cryst. Growth Des.* **2017**, *17*, 2730–2735. [[CrossRef](#)]
27. Zheng, H.; Zhang, J.; Wang, B.; Phelan, D.; Krogstad, M.J.; Ren, Y.; Phelan, W.A.; Chmaissem, O.; Poudel, B.; Mitchell, J.F. High pO<sub>2</sub> Floating Zone Crystal Growth of the Perovskite Nickelate PrNiO<sub>3</sub>. *Crystals* **2019**, *9*, 324. [[CrossRef](#)]
28. Phelan, W.A.; Zahn, J.; Kennedy, Z.; McQueen, T.M. Pushing boundaries: High pressure, supercritical optical floating zone materials discovery. *J. Solid State Chem.* **2018**, *270*, 705–709. [[CrossRef](#)]
29. Azuma, M.; Saito, T.; Ishiwata, S.; Yamada, I.; Kohsaka, Y.; Takagi, H.; Takano, M. Single crystal growth of transition metal oxides at high pressures of several GPa. *Physica C* **2003**, *392–396 Pt 1*, 22–28. [[CrossRef](#)]
30. Masaki, A.; Takashi, S.; Shintaro, I.; Hirofumi, Y.; Mikio, T.; Yuhki, K.; Hidenori, T.; Wataru, U. Single-crystal growth of transition metal oxides at high pressures of several GPa. *J. Phys. Condens. Matter* **2002**, *14*, 11321.
31. Alonso, J.A.; Muñoz, A.; Largeteau, A.; Demazeau, G. Crystal growth of NdNiO<sub>3</sub> perovskite under high oxygen pressure. *J. Phys. Condens. Matter* **2004**, *16*, S1277. [[CrossRef](#)]
32. Puphal, P.; Wu, Y.-M.; Fürsich, K.; Lee, H.; Pakdaman, M.; Bruin, J.A.N.; Nuss, J.; Suyolcu, Y.E.; Aken, P.A.v.; Keimer, B.; et al. Topotactic transformation of single crystals: From perovskite to infinite-layer nickelates. *Sci. Adv.* **2021**, *7*, eabl8091. [[CrossRef](#)]
33. Klein, Y.M.; Kozłowski, M.; Linden, A.; Lacorre, P.; Medarde, M.; Gawryluk, D.J. RENiO<sub>3</sub> Single Crystals (RE = Nd, Sm, Gd, Dy, Y, Ho, Er, Lu) Grown from Molten Salts under 2000 bar of Oxygen Gas Pressure. *Cryst. Growth Des.* **2021**, *21*, 4230–4241. [[CrossRef](#)]
34. Bruker APEX2; Bruker Analytical X-ray Instruments Inc: Madison, WI, USA, 2014.
35. Prakash, J.; Blakely, C.K.; Poltavets, V.V. Low temperature high-pressure synthesis of LnNiO<sub>3</sub> (Ln = Eu, Gd) in molten salts. *Solid State Sci.* **2013**, *17*, 72–75. [[CrossRef](#)]
36. Song, Y.T.; Peng, J.B.; Wang, X.; Sun, G.L.; Lin, C.T. Ambient-condition growth of superconducting YBa<sub>2</sub>Cu<sub>4</sub>O<sub>8</sub> single crystals using KOH flux. *J. Cryst. Growth* **2007**, *300*, 263–266. [[CrossRef](#)]
37. de Brion, S.; Bonda, M.; Darie, C.; Bordet, P.; Sheikin, I. Magnetic phase diagram of the S = 1/2 triangular layered compound NaNiO<sub>2</sub>: A single crystal study. *J. Phys. Condens. Matter* **2010**, *22*, 126001. [[CrossRef](#)]
38. Wang, B.-X.; Zheng, H.; Kriviyakina, E.; Chmaissem, O.; Lopes, P.P.; Lynn, J.W.; Gallington, L.C.; Ren, Y.; Rosenkranz, S.; Mitchell, J.F.; et al. Synthesis and characterization of bulk Nd<sub>1-x</sub>Sr<sub>x</sub>NiO<sub>2</sub> and Nd<sub>1-x</sub>Sr<sub>x</sub>NiO<sub>3</sub>. *Phys. Rev. Mater.* **2020**, *4*, 084409. [[CrossRef](#)]
39. Fujihara, S.; Murakami, G.; Kimura, T. Oxygen deficiency and electrical conductivity of Nd<sub>1-x</sub>A<sub>x</sub>NiO<sub>3-y</sub> (A = alkaline earth) prepared by the low-temperature process. *J. Alloys Compd.* **1996**, *243*, 70–76. [[CrossRef](#)]
40. Catalan, G. Progress in perovskite nickelate research. *Phase Transit.* **2008**, *81*, 729–749. [[CrossRef](#)]

41. Lorenzo, J.E.; Hodeau, J.L.; Paolasini, L.; Lefloch, S.; Alonso, J.A.; Demazeau, G. Resonant X-ray scattering experiments on electronic orderings in NdNiO<sub>3</sub> single crystals. *Phys. Rev. B* **2005**, *71*, 045128. [[CrossRef](#)]
42. García-Muñoz, J.L.; Aranda, M.A.G.; Alonso, J.A.; Martínez-Lope, M.J. Structure and charge order in the antiferromagnetic band-insulating phase of NdNiO<sub>3</sub>. *Phys. Rev. B* **2009**, *79*, 134432. [[CrossRef](#)]

**Disclaimer/Publisher's Note:** The statements, opinions and data contained in all publications are solely those of the individual author(s) and contributor(s) and not of MDPI and/or the editor(s). MDPI and/or the editor(s) disclaim responsibility for any injury to people or property resulting from any ideas, methods, instructions or products referred to in the content.